Mon. Not. R. Astron. Soc. **383,** 263–276 (2008) doi:10.1111/j.1365-2966.2007.12528.x

Anatomy of a young massive star cluster: NGC 1569-B⋆

S. S. Larsen,[1]† L. Origlia,[2]† J. Brodie[3]† and J. S. Gallagher, III[4]†

[1]*Astronomical Institute, University of Utrecht, Princetonplein 5, NL-3584 CC Utrecht, the Netherlands*
[2]*INAF – Osservatorio Astronomico di Bologna, Via Ranzani 1, I-40127 Bologna, Italy*
[3]*UCO/Lick Observatory, 1156 High Street, University of California, Santa Cruz, CA 95064, USA*
[4]*Astronomy Department, University of Wisconsin, 475 North Charter Street, Madison, WI 53706, USA*

Accepted 2007 October 2. Received 2007 October 2; in original form 2007 September 13

ABSTRACT

We present new *H*-band echelle spectra, obtained with the NIRSPEC spectrograph at Keck II, for the massive star cluster 'B' in the nearby dwarf irregular galaxy NGC 1569. From spectral synthesis and equivalent width measurements, we obtain abundances and abundance patterns. We derive an Fe abundance of [Fe/H] $= -0.63 \pm 0.08$, a supersolar [α/Fe] abundance ratio of $+0.31 \pm 0.09$, and an O abundance of [O/H] $= -0.29 \pm 0.07$. We also measure a low $^{12}C/^{13}C \approx 5 \pm 1$ isotopic ratio. Using archival imaging from the Advanced Camera for Surveys onboard the *Hubble Space Telescope* (*HST*), we construct a colour–magnitude diagram (CMD) for the cluster in which we identify about 60 red supergiant (RSG) stars, consistent with the strong RSG features seen in the *H*-band spectrum. The mean effective temperature of these RSGs, derived from their observed colours and weighted by their estimated *H*-band luminosities, is 3790 K, in excellent agreement with our spectroscopic estimate of $T_{\rm eff} = 3800 \pm 200$ K. From the CMD, we derive an age of 15–25 Myr, slightly older than previous estimates based on integrated broad-band colours. We derive a radial velocity of $\langle v_{\rm r} \rangle = -78 \pm 3$ km s^{-1} and a velocity dispersion of 9.6 ± 0.3 km s^{-1}. In combination with an estimate of the half-light radius of 0.20 ± 0.05 arcsec from the *HST* data, this leads to a dynamical mass of $(4.4 \pm 1.1) \times 10^5$ M$_\odot$. The dynamical mass agrees very well with the mass predicted by simple stellar population models for a cluster of this age and luminosity, assuming a normal stellar initial mass function. The cluster core radius appears smaller at longer wavelengths, as has previously been found in other extragalactic young star clusters.

Key words: techniques: spectroscopic – supergiants – galaxies: abundances – galaxies: individual: NGC 1569 – galaxies: star clusters – infrared: galaxies.

1 INTRODUCTION

Massive star clusters are potentially useful test particles for constraining the evolutionary histories of their host galaxies. They can remain observable for the entire lifetime of a galaxy (as illustrated by the old *globular clusters* which surround every major galaxy), and they are bright enough to be studied in detail well beyond the Local Group. The internal velocity broadening of their spectra is typically only a few km s^{-1}, making detailed abundance analysis at high spectral resolution feasible. In a previous paper, we have taken a first step towards exploiting this potential by analysing *H*- and *K*-band spectra of a young massive star cluster (YMC) in the nearby spiral galaxy NGC 6946 (Larsen et al. 2006). Here, we apply a similar analysis to one of the young star clusters in the nearby (post-) starburst galaxy NGC 1569.

NGC 1569 was one of the first galaxies in which the presence of exceptionally bright, young star clusters was suspected. A spectrum of one of the two bright 'stellar condensations' in NGC 1569 was obtained already by Mayall (1935), although the true nature of these objects was probably first discussed in detail by Arp & Sandage (1985). They found that the spectra are of composite nature, and also noted that observations with the *Hubble Space Telescope* (*HST*) would definitively settle the issue whether or not these objects are really 'super star clusters'. Indeed, pre-refurbishment mission *HST*

⋆Based in part on data obtained at the W. M. Keck Observatory, which is operated as a scientific partnership among the California Institute of Technology, the University of California, and the National Aeronautics and Space Administration (NASA). The Observatory was made possible by the generous financial support of the W. M. Keck Foundation. Also based on observations with the NASA/ESA *Hubble Space Telescope*, obtained from the data archive at the Space Telescope Science Institute (STScI). STScI is operated by the association of Universities for Research in Astronomy, Incorporated, under the NASA contract NAS 5-26555.
†E-mail: larsen@astro.uu.nl (SSL); livia.origlia@bo.astro.it (LO); brodie@ucolick.org (JB); jsg@astro.wisc.edu (JSG)

observations by O'Connell, Gallagher & Hunter (1994) settled the issue by showing that both objects are extended, with half-light radii of about 2 pc. Based on high-dispersion spectroscopy from the HIRES spectrograph on the Keck I telescope, a dynamical mass of $\approx 10^6\,M_\odot$ was soon after estimated for the brighter of the two objects, NGC 1569-A (Ho & Filippenko 1996; Sternberg 1998).

The clusters in NGC 1569 are prime candidates for abundance analysis in the near-infrared (near-IR) where they are very bright. The IR holds a particular advantage over optical studies for NGC 1569 due to the large amount of foreground extinction. Gilbert & Graham (2002) found the integrated *H*-band spectra of both clusters A and B to be well approximated by red supergiant (RSG) templates. Although NGC 1569-A is the brighter of the two, it is actually a binary cluster itself with some evidence for a (small) age difference between the two components (de Marchi et al. 1997; Maoz, Ho & Sternberg 2001; Origlia et al. 2001). Whether or not the two components are physically connected or the result of a chance projection is unknown. In this paper, we concentrate on NGC 1569-B.

In addition to providing insight into the histories of their host galaxies, young star clusters with masses in excess of $10^5\,M_\odot$ also offer an excellent opportunity to study large samples of coeval massive stars. Such clusters are rare in the Milky Way and even in the Local Group, so it is necessary to extend the search to a larger volume. The most-massive known young star clusters in the Milky Way disc are Westerlund 1 (Clark et al. 2005) and an object discovered in the 2MASS (Figer et al. 2006), both of which may have masses approaching $10^5\,M_\odot$. Young clusters of similar masses are found in the Large Magellanic Cloud (LMC; van den Bergh 1999), but these pale in comparison with objects like NGC 1569-A and NGC 1569-B.

We have obtained new NIRSPEC *H*-band spectra of NGC 1569-B, optimized for abundance analyses, and we additionally present photometry for *individual* stars in the cluster derived from archival observations with the high-resolution channel (HRC) of the Advanced Camera for Surveys (ACS) onboard *HST*. The *HST* data provide an independent verification of the stellar parameters (notably $T_{\rm eff}$ and $\log g$) derived from the spectral analysis, and also allow us to compare the observed colour–magnitude diagram (CMD) with standard isochrones. Finally, we use new measurements of the structural parameters and velocity dispersion to derive the cluster mass and mass-to-light ratio and compare with predictions by simple stellar population (SSP) models.

We begin by briefly describing the data in Section 2. The analysis and our main results then follow in Section 3, where we first discuss the near-IR spectroscopy and the abundance analysis (Section 3.1). We then proceed to construct a CMD from the *HST* imaging (Section 3.2) from which we derive stellar parameters for the RSGs that are compared against the spectroscopic results (Section 3.2.3) and theoretical isochrones (Section 3.2.4). In Section 3.3, we measure structural parameters for NGC 1569-B and combine these with velocity dispersion measurements to derive a dynamical mass estimate. Finally, some additional discussion and a summary are given in Section 4.

2 DATA

2.1 NIRSPEC data

We observed NGC 1569-B in the *H* band with the NIRSPEC spectrograph (McLean et al. 1998) on the Keck II telescope on 2006 November 8, using the high-resolution echelle mode with a slit width of 0.432 arcsec (3 pixel). This yields a spectral resolution of $\lambda/\Delta\lambda = 25\,000$. Since the NIRSPEC detector does not cover the entire *H*-band echellogram in a single exposure, we optimized the tilts of the NIRSPEC gratings so that the number of features suitable for abundance determination was maximized. To facilitate easy sky-subtraction, we followed the standard strategy of obtaining pairs of exposures nodded a few arcseconds along the slit. A total of 20 integrations, each with an exposure time of 300 s, were made, resulting in a total exposure time of 6000 s. One-dimensional spectra were extracted from each pair of nodded exposures and wavelength-calibrated using the REDSPEC IDL package written by L. Prato, S. S. Kim and I. S. McLean. The individual one-dimensional spectra were then co-added. The final summed one-dimensional spectra have a signal-to-noise ratio (S/N) of about 100 per pixel, or $\sim$175 per 3 pixel resolution element.

2.2 HST/ACS data

We use observations of NGC 1569 obtained with the ACS HRC as part of programme GTO-9300 (P.I.: H. Ford). The HRC has a field of view of about $29 \times 26\,{\rm arcsec}^2$ and a pixel scale of $\sim$0.027 arcsec pixel^{-1}, but with significant variations across the field due to the geometric distortions in ACS. For the photometry of individual stars. we use the *F555W* ($\approx V$ band) and *F814W* ($\approx I$-band) images, each exposed for 3×130 s. For measurements of structural parameters, we also include *F330W* ($\approx U$ band) data (3×220 s). The data were downloaded from the *HST* archive at the Space Telescope-European Coordinating Facility (ST-ECF) and individual exposures were co-added with the MULTIDRIZZLE task (Koekemoer et al. 2002). MULTIDRIZZLE filters out cosmic-ray hits and detector defects, corrects for geometric distortions and projects the images on an orthogonal pixel grid with a scale of exactly 0.025 arcsec pixel^{-1}. At a distance of 2.2 Mpc (Section 2.3), this corresponds to a linear scale of 0.27 pc pixel^{-1}.

2.3 Distance and reddening of NGC 1569

While it is clear from the high degree of resolution into individual stars that NGC 1569 must be nearby, the exact distance remains quite uncertain. One uncertainty is in the correction for foreground extinction, for which the NASA Extragalactic Database (NED) gives either $A_B = 2.03$ mag (Burstein & Heiles 1982) or $A_B = 3.02$ mag (Schlegel, Finkbeiner & Davis 1998). Israel (1988) estimated $E(B-V) = 0.56 \pm 0.10$ or $A_B = 2.30 \pm 0.40$ mag (for $R_B = 4.1$). Combined with the apparent distance modulus $(m-M)_B = 29.0$ derived by Arp & Sandage (1985), this leads to $(m-M)_0 = 26.7 \pm 0.6$ or $D = 2.2 \pm 0.6$ Mpc, which is the value used by Origlia et al. (2001) and several other studies in the literature. Based on photometry for a small number of yellow supergiants (YSGs) and blue supergiants (BSGs) and also using $E(B-V) = 0.56$, O'Connell et al. (1994) estimated $D = 2.5 \pm 0.5$ Mpc. Using observations of the red giant branch tip, Makarova & Karachentsev (2003) derived two possible distances of either $D = 1.95 \pm 0.2$ or 2.8 ± 0.2 Mpc, both assuming the Schlegel et al. foreground extinction. For the lower Israel (1988) extinction, the distances would instead be $D = 2.7 \pm 0.3$ or 3.9 ± 0.3 Mpc. In this paper, we use the same value of 2.2 Mpc as used by Origlia et al. (2001) and the extinction value from Israel (1988), that is, $E(B-V) = 0.56$ or $A_B = 2.30$ mag ($A_V = 1.74$ mag). The abundance analysis is not affected by either of these parameters. For the analysis of the CMD and the cluster mass, we will give further comments when needed.

3 ANALYSIS AND RESULTS

3.1 Chemical abundances

In general, abundance analysis from integrated spectra requires full spectral synthesis techniques to properly account for line blending and population synthesis to define the dominant contribution to the stellar luminosity. The near-IR stellar continuum of young stellar clusters and starburst galaxies is almost entirely due to luminous RSGs (see e.g. Origlia & Oliva 2000, for a review) and usually it dominates over nebular and dust emission. This represents a major, conceptual simplification in population and spectral synthesis techniques, making the interpretation of integrated spectra much easier. The spectra can be modelled with an equivalent, average star, whose stellar parameters (temperature $T_{\rm eff}$, gravity $\log g$ and microturbulence velocity ξ) mainly depend on the age and metallicity.

Our analysis of the NIRSPEC spectra of NGC 1569-B closely followed that in our study of a YMC in NGC 6946 (Larsen et al. 2006). A grid of synthetic RSG spectra for different input atmospheric parameters and abundances were computed, using an updated (Origlia, Rich & Castro 2002; Origlia et al. 2003) version of the code described in Origlia, Moorwood & Oliva (1993). Briefly, the code uses the local thermodynamic equilibrium approximation and is based on molecular blanketed model atmospheres of Johnson, Bernat & Krupp (1980) at temperatures $\leq$4000 K. Recently, the NEXTGEN model atmospheres (Hauschildt et al. 1999) have been also implemented within the code and tested, yielding very similar results. The code also includes several thousands of near-IR atomic lines and molecular rotovibrational transitions due to CO, OH and CN. Three main compilations of atomic oscillator strengths are used, namely the Kurucz data base[1] and those published by Bièmont & Grevesse (1973) and Meléndez & Barbuy (1999). For further details, we refer to Origlia et al. (1993, 2002) and Origlia et al. (2003).

As was done for the YMC in NGC 6946, we estimated the random errors on the derived quantities using a number of test models. With respect to the best-fitting spectrum, we varied the temperature by $\Delta T_{\rm eff}$ of $\pm$200 K, the microturbulence by $\Delta\xi$ of $\mp$1.0 km s^{-1}, gravity by $\Delta\log g$ of $\pm$0.5 dex and abundances varying accordingly by $\approx \pm$0.2 dex, in order to still reproduce the depth of the observed features. By comparing the mean difference (δ) between the observed and best-fitting model spectrum with the corresponding δ-value for each test model, we found that the test models are at best statistically significant at $\geq 2\sigma$ level, only. See Larsen et al. (2006) for details.

Fig. 1 shows several regions of the cluster spectrum with the most-prominent features indicated. As noted in several previous studies, the spectrum shows many absorption features indicating the presence of RSGs. The open circles are the observed spectrum, the solid lines are the best-fitting RSG model spectrum and the dotted lines are models with a factor of 2 different abundances from the best-fitting solution. Synthetic spectra with lower element abundances are *systematically* shallower than the best-fitting solution, while the opposite occurs when higher abundances are adopted.

By fitting the full observed *H*-band spectrum and by measuring the equivalent widths of selected lines, we obtained the stellar parameters and abundance patterns listed in Table 1. Reference solar abundances are from Grevesse & Sauval (1998). Among the measured quantities are an Fe abundance of [Fe/H] $= -0.63 \pm 0.08$ and [O/H] $= -0.29 \pm 0.07$ (i.e. $12 + \log({\rm O/H}) = 8.54$), which combine to [O/Fe] $= 0.34 \pm 0.10$. We also measure an average [α/Fe] $= 0.31 \pm 0.09$ enhancement for the other α-elements and $^{12}{\rm C}/^{13}{\rm C} \approx 5 \pm 1$. The latter ratio is even lower than the value we found for the YMC in NGC 6946 ($^{12}{\rm C}/^{13}{\rm C} = 8 \pm 2$). Isotopic $^{12}{\rm C}/^{13}{\rm C}$ abundance ratios below 10 are quite common in Galactic RSGs (Lambert & Tomkin 1974; Tomkin, Luck & Lambert 1976; Gonzalez & Wallerstein 2000) and have also been found in the cluster NGC 330 in the Small Magellanic Cloud (SMC; Gonzalez & Wallerstein 1999). The fact that the observed $^{12}{\rm C}/^{13}{\rm C}$ values in RSGs tend to be lower than standard stellar models predict (Schaller et al. 1992) may indicate that extra mixing mechanisms are present.

To our knowledge, no previous determination of the Fe abundance in NGC 1569 exists. Our value is similar to that of cool supergiants in the SMC (Hill 1999). Our oxygen abundance for NGC 1569-B, on the other hand, is more similar to that of young stars in the LMC, although the number of stars with reliable abundance determinations is small (Rolleston, Trundle & Dufton 2002). Our O abundance for NGC 1569-B is about a factor of 2 higher than the commonly cited value of $12 + \log({\rm O/H}) = 8.19 \pm 0.02$ for H II regions in NGC 1569 (Kobulnicky & Skillman 1997). Other measurements of the O abundance in NGC 1569 come from Storchi-Bergmann, Calzetti & Kinney (1994) who derived $12 + \log({\rm O/H}) = 8.37$, intermediate between our value and that of Kobulnicky & Skillman (1997), while Devost, Roy & Drissen (1997) got $12 + \log({\rm O/H}) = 8.26$. All these previous measurements refer to the ionized gas, however, and we are not aware of any previous measurement of the O abundance in NGC 1569 from stellar spectroscopy.

From the spectral fits, we also measure a heliocentric radial velocity of $\langle v_{\rm r}\rangle = -78 \pm 3$ km s^{-1} and velocity dispersion (corrected for instrumental broadening) of $\approx$9.9 $\pm$ 1 km s^{-1}. This velocity dispersion is higher than 7.5 $\pm$ 0.2 km s^{-1} found by Gilbert & Graham (2002), but agrees well with our measurement based on cross-correlation analysis (Section 3.3.4). The radial velocity itself is in excellent agreement with the optical radial velocity of NGC 1569 listed in the Third Reference Catalogue of Bright Galaxies (-74 ± 17 km s^{-1}; de Vaucouleurs et al. 1991).

3.2 The cluster colour–magnitude diagram

3.2.1 Photometry

The HRC images show NGC 1569-B resolved into its brightest constituent stars. This presents us with a welcome opportunity to check the properties of RSGs derived from the spectral fits. To study the CMD, we therefore carried out point spread function (PSF)-fitting photometry with the DAOPHOT III photometry package (Stetson 1987, 1990). Stars were first detected in the *F814W* image with the FIND task, aperture photometry was obtained for the *F555W* and *F814W* images with the PHOT task and PSFs were constructed using seven isolated stars scattered across the HRC detector. A first iteration of PSF-fitting photometry was then carried out by running the ALLFRAME task on the *F555W* and *F814W* frames simultaneously. The FIND routine was applied a second time to the star-subtracted *F814W* image produced by ALLFRAME, and improved PSFs were constructed by running the PSF task once again on images where all stars detected in the first pass (except the PSF stars) had been subtracted. The ALLFRAME PSF fitting was then repeated with the combined coordinate list. We found that two such iterations were sufficient to produce very clean final star-subtracted images. Fig. 2 shows the *F814W* image of NGC 1569-B in the left-hand panel and the residual image produced by the second ALLFRAME iteration in the right-hand panel. The stars subtract out

[1] http://cfa-www.harward.edu/amdata/ampdata/kurucz23/sekur.html

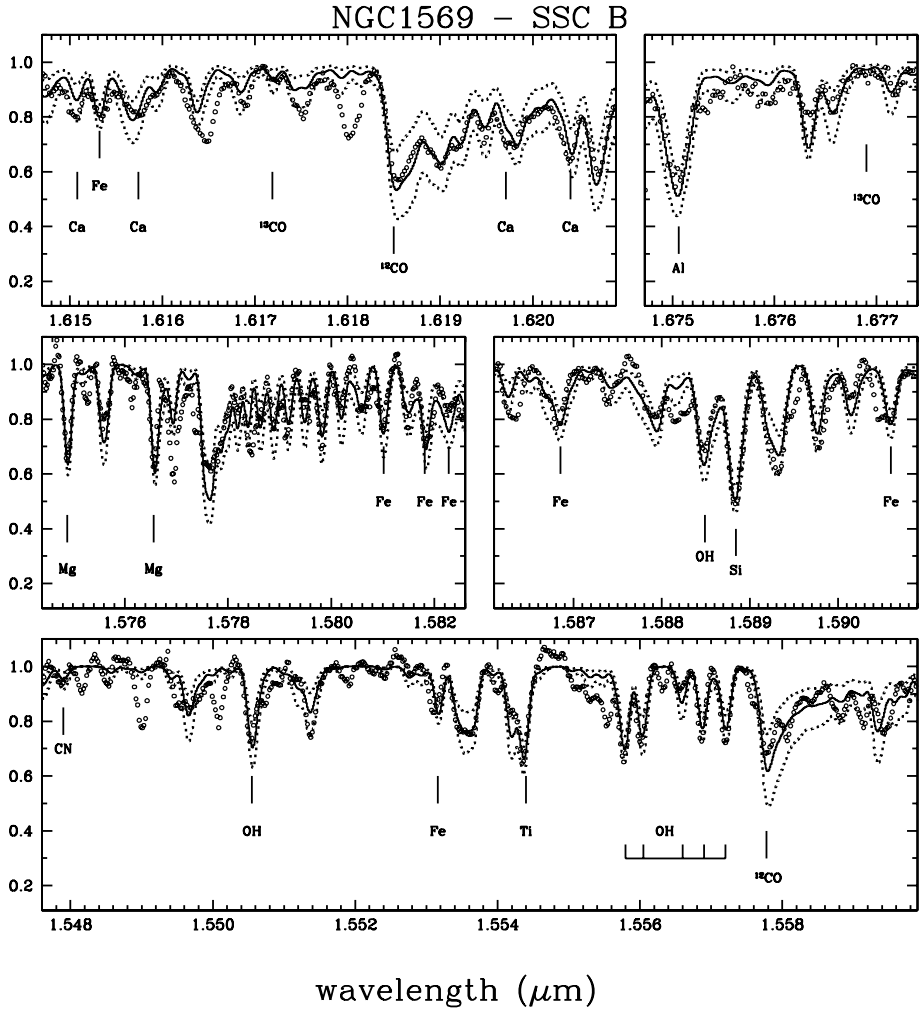

Figure 1. Near-IR spectra of the SSC B of NGC 1569. Observed spectrum: open circles. Solid line: best-fitting RSG spectrum. Dotted lines: model spectra with abundances scaled by a factor of 0.5 and 2.0. A few atomic and molecular features of interest are also marked.

Table 1. Adopted stellar atmosphere parameters and abundance estimates for cluster B in NGC 1569.

$T_{\rm eff}$ (K)	$\log g$	ξ (km s^{-1})	[Fe/H]	[O/Fe]	[Ca/Fe]	[Si/Fe]	[Mg/Fe]	[Ti/Fe]	[α/Fe]^a	[Al/Fe]	[C/Fe]
3800	0.0	3	−0.63	0.34	0.33	0.33	0.23	0.33	0.31	0.23	−0.27
±200	±0.5		±0.08	±0.10	±0.09	±0.11	±0.13	±0.10	±0.09	±0.11	±0.10

^{a}[α/Fe] is the average [⟨Ca, Si, Mg, Ti⟩/Fe] abundance ratio.

nicely without any systematic residuals, even quite close to the centre of the cluster, indicating that the PSF-fitting procedure went well.

For calibration to the VEGAMAG system, we used the photometric zero-points for the HRC published on the ACS WWW ($z_{F555W} = 25.255$ mag, $z_{F814W} = 24.849$ mag). To fix the zero-points of the PSF-fitting photometry, we carried out aperture photometry in a radius of 5 pixel (0.125 arcsec) for a number of bright stars on images where all other stars had been subtracted and calculated the offset between the aperture and PSF photometry for these stars. We estimate that the uncertainty in tying the PSF and aperture photometry together is about 0.01–0.02 mag. The aperture corrections from 5 pixel to infinity were taken from the tables of encircled energy distributions in Sirianni et al. (2005).

3.2.2 *Completeness and contamination*

The resulting CMD is shown in Fig. 3 for the radial range $15 < R < 50$ pixel ($0.37 < R < 1.25$ arcsec). Closer to the centre, the crowding becomes too severe to obtain useful photometry and farther out contamination from the general field population becomes an increasing worry. Our CMD is consistent with the one already shown by Hunter et al. (2000), who used data from the Wide Field Planetary Camera 2 (WFPC2), in containing a large number of RSGs.

The severe crowding requires that careful attention be paid to completeness effects. We quantified the detection incompleteness and photometric errors by adding artificial stars in the same annulus for which the CMD was constructed. A common procedure when

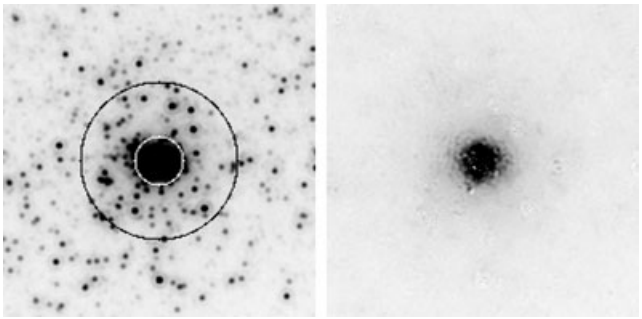

Figure 2. Left-hand panel: ACS/HRC *F814W* image of NGC 1569-B. The circles indicate the region for which a CMD was constructed. Right-hand panel: the residual image produced by DAOPHOT/ALLFRAME.

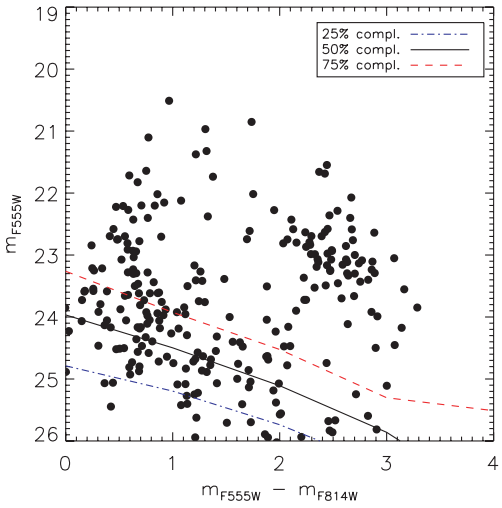

Figure 3. CMD for NGC 1569-B. The three curves show the 75 per cent (dashed line, red in the online edition), 50 per cent (solid line) and 25 per cent (dot–dashed line, blue in the online edition) completeness limits based on artificial star experiments.

carrying out such artificial object tests is to add stars at random positions within an image; however, it is not necessary that the positions are truly random. As long as the underlying distribution of stars is random itself, no loss of generality results from adding the artificial stars in a semi-regular grid. The advantage is that they can be more closely packed this way. The only caveat is that care must be taken to sample different positions of the PSF at the subpixel level, in particular for undersampled images such as those from *HST*. We distributed the artificial stars in concentric rings with a radial separation of 10 pixel between each ring and a separation of 10 pixel between stars within each ring. This approach automatically provides the required (pseudo-) randomness of the PSF positions at subpixel level and ensures that no two artificial stars are closer together than 10 pixel, thus avoiding 'self-crowding' of the artificial stars.

The artificial stars were recovered using exactly the same procedure as for the regular photometry. In order to sample the incompleteness in different regions of the CMD, artificial stars with magnitudes between $m_{F555W} = 20.0$ and $m_{F555W} = 26.0$ (in steps of 0.5 mag) and colours between $m_{F555W} - m_{F814W} = 0.0$ and $m_{F555W} - m_{F814W} = 4.0$ (in steps of 1 mag) were added. By repeating the procedure five times, each with a different origin of the grid, we could sample a total of 346 artificial stars at every magnitude and

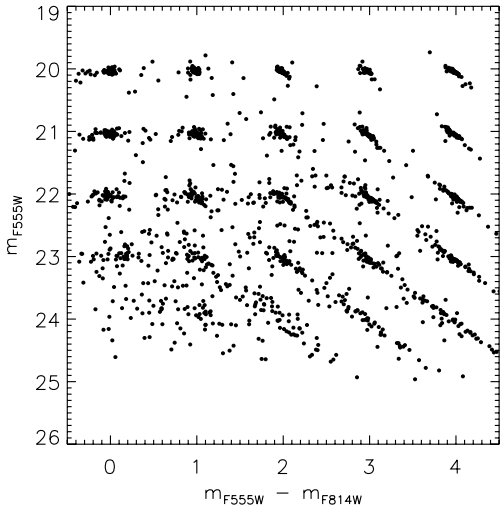

Figure 4. CMD for artificial objects after recovery and PSF-fitting photometry. Objects with input magnitudes of $m_{F555W} = 20, 21, \ldots, 24$ and $m_{F555W} - m_{F814W} = 0, 1, 2, 3, 4$ are shown here.

colour within the annulus used for the photometry, allowing us to quantify the detection completeness with good statistical accuracy.

Fig. 4 shows the CMD for the recovered objects. For clarity, every second magnitude step has been omitted, and only one of the five tests at each colour/magnitude is shown. A comparison with Fig. 3 shows that the concentration of RSGs at $m_{F555W} - m_{F814W} \approx 2.5$ and $m_{F555W} \approx 23$ is real and not just an artefact of incompleteness towards fainter magnitudes. If any significant number of red objects with $m_{F555W} \approx 24$ were present, they would be clearly detected. On the other hand, in the blue part of the CMD the fainter magnitude limit appears to be predominantly a detection limit. To put these statements on a firmer ground, we used the output from the completeness tests to calculate the magnitudes at which 25, 50 and 75 per cent of the artificial objects were recovered as a function of colour. These limits are shown in Fig. 3 and confirm that the concentration of RSGs is found well above any of these limits. The lower envelope of the remaining data points is consistent with the completeness limits inferred from the artificial star experiments. We conclude that the RSGs, which dominate the near-IR spectra, are well sampled by the ACS/HRC data, and we can use the photometry to constrain their properties further.

The artificial star tests also show that much of the scatter in the colours of the RSGs can be accounted for by photometric errors. Because the errors on the $m_{F555W} - m_{F814W}$ colours are dominated by the errors on m_{F555W} for red objects, the recovered artificial star magnitudes at the position of the RSGs scatter along a line which is nearly diagonal in the CMD. A similar trend is seen in the observed CMD in Fig. 3. This suggests that the RSGs in NGC 1569-B span a fairly narrow intrinsic range in the $m_{F555W} - m_{F814W}$ colour, and hence in $T_{\rm eff}$.

Before proceeding, the question of contamination of the cluster CMD by the general field population of NGC 1569 must be addressed. Crowding prevents us from measuring stars closer than about 0.38 arcsec from the centre of the cluster, which is about twice the half-light radius. In the top panel of Fig. 5, we again show the CMD within $0.38 < R < 1.25$ arcsec, now corrected for Galactic extinction and converted to an absolute magnitude scale. The centre panel shows the CMD for a larger annulus with the same area. Completeness effects are expected to be less severe in this less-crowded

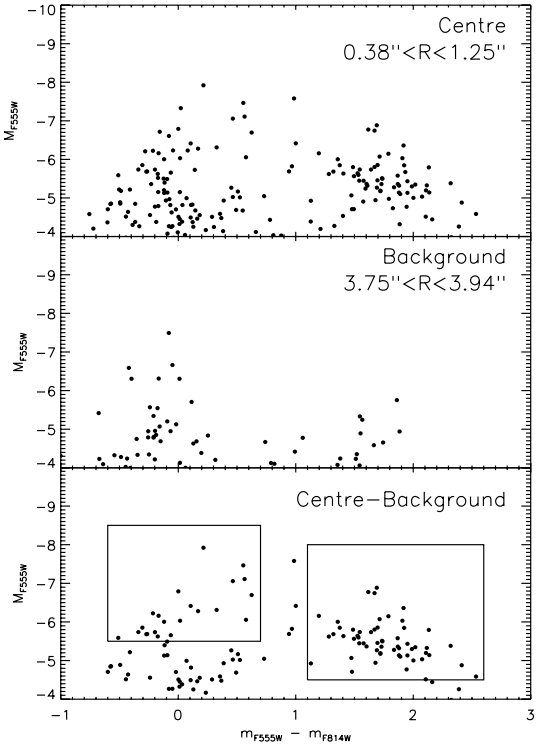

Figure 5. Statistical decontamination of the CMD for NGC 1569-B. Top panel: the CMD for the annulus illustrated in Fig. 2. Centre panel: the CMD for an annulus of larger radius, but identical surface area. Bottom panel: sources in the central panel which have a match within 0.5 mag in the top panel have been subtracted from the top panel.

region, yet the population of RSGs is virtually absent. This supports the notion that the RSGs in the top panel are indeed predominantly associated with cluster B as also concluded by Hunter et al. (2000). The bottom panel shows the statistical difference between the top and centre panels, constructed by removing every star in the central annulus which has a matching data point within 0.5 mag in m_{F555W} and m_{F814W} in the background annulus. For the RSGs, there is no significant difference, although some fraction of the blue stars are removed. Since we have not applied separate completeness corrections in the two annuli, it is likely that too many blue stars have been subtracted near the detection limit.

3.2.3 Comparison with spectroscopy

Within the right-hand selection box in the bottom panel of Fig. 5, we find 57 RSGs with a mean colour of $\langle M_{F555W} - M_{F814W} \rangle = 1.75$ and $\langle M_{F555W} \rangle = -5.6$. For each star, we can estimate the effective temperature and bolometric corrections from the observed $M_{F555W} - M_{F814W}$ colour, by using conversions computed with the code described by Origlia & Leitherer (2000) and multiplying the model atmospheres by Bessel, Castelli & Plez (1998) with the ACS filter responses. This yields $\langle T_{\rm eff} \rangle = 3850$ K, very close to the estimate of $T_{\rm eff} = 3800 \pm 200$ K obtained from the spectral analysis. If we instead calculate the $T_{\rm eff}$ values individually for each star and then compute an average weighted by the estimated H-band luminosity of each star, cooler stars will receive greater weights and the average $T_{\rm eff}$ decreases to $\langle T_{\rm eff} \rangle = 3790$ K, again in excellent agreement with the spectroscopic estimate.

Different assumptions about the distance will not affect the photometric estimate of $T_{\rm eff}$, although different assumptions about extinction clearly will. If instead of $A_B = 2.30$ we assume $A_B = 3.02$ (Schlegel et al. 1998), then $T_{\rm eff}$ increases by about 200 K.

Table 2. Observed and model supergiant properties. BSG/RSG is the ratio of BSGs to RSGs and $\langle T_{\rm eff} \rangle_{\rm RSG}$ is the mean effective temperature of RSGs, weighted by their absolute M_{F555W} magnitude. RSGs are here defined as stars having $M_{F555W} < -4.5$ and $M_{F555W} - M_{F814W} > 1.1$.

	BSG/RSG	$\langle T_{\rm eff} \rangle_{\rm RSG}$ (K)
Observed	0.39 ± 0.10	3850
Padua $Z = 0.008$		
$\log t = 7.0$	1.75	4130
$\log t = 7.2$	1.70	4110
$\log t = 7.4$	0.80	4100
Geneva $Z = 0.008$		
$\log t = 7.0$	0.29	3870
$\log t = 7.2$	3.29	3950
$\log t = 7.4$	1.10	3970
Padua $Z = 0.004$		
$\log t = 7.0$	1.50	4350
$\log t = 7.2$	2.42	4290
$\log t = 7.4$	0.81	4310
Geneva $Z = 0.004$		
$\log t = 7.0$	8.69	4270
$\log t = 7.2$	33.7	4110
$\log t = 7.4$	2.67	4200

Having estimated the mean absolute magnitude and effective temperature of the RSGs from the CMD, the stellar diameter follows and we can estimate the surface gravity if the mass is known. For an age of $\log t = 7.3$ (Section 3.2.4), isochrones from the Padua group (Girardi et al. 2000) give a turn-off mass of $12.4\,{\rm M}_\odot$. Assuming $T_{\rm eff} = 3800$ K, we get a bolometric correction of -1.4 mag from the Kurucz models[2]. The mean RSG luminosity is then $L_{\rm RSG}/{\rm L}_\odot = 4.9 \times 10^4$ and the radius is $R_{\rm RSG}/{\rm R}_\odot = 510$, which leads to $\log g = 0.1$ (in cgs units). This is again very close to the value $\log g = 0.0$ derived from the RSG model spectral fit.

3.2.4 Model comparison and the ratio of blue to red supergiants

Models for massive stars are still fraught with significant uncertainties, partly because there is still only a limited amount of data available to compare with. CMDs for YMCs such as NGC 1569-B can help constrain the models.

The mean effective temperature of RSGs predicted by models from the Padua and Geneva (Lejeune & Schaerer 2001) groups are listed in Table 2 for two different metallicities: $Z = 0.004$ and 0.008. The Geneva models are available for 'standard' and 'enhanced' mass-loss rates. Here, we use the models with enhanced mass loss since these compare most favourably with the data. We have selected the RSGs in the same way as for the empirical data, that is, RSGs are here defined as stars with $M_{F555W} - M_{F814W} > 1.1$. The $\langle T_{\rm eff} \rangle_{\rm RSG}$ values in Table 2 are the average of the $T_{\rm eff}$ values listed in the isochrone tables for these stars, weighted by the luminosity in *F555W* and the number of stars at each initial mass according to a Kroupa (2002) initial mass function (IMF). Because all RSGs have very nearly the same mass for a given age, it makes virtually no difference what IMF is actually assumed and even for

[2] Downloaded from http://kurucz.harvard.edu/grids.html

a flat IMF the mean effective temperature would change by only a few K. In all cases, the models predict the RSGs to be hotter than observed, with the $Z = 0.008$ Geneva isochrones coming closest to matching the observations in this respect. The $Z = 0.008$ Geneva models for standard mass loss produce RSGs which are about 100 K hotter than the enhanced mass-loss models for the two youngest ages, while for the $Z = 0.004$ models (which are less affected by mass loss) there is no difference.

In Figs 6 and 7, we compare our background-subtracted CMD with the theoretical isochrones. Rather than simply drawing the

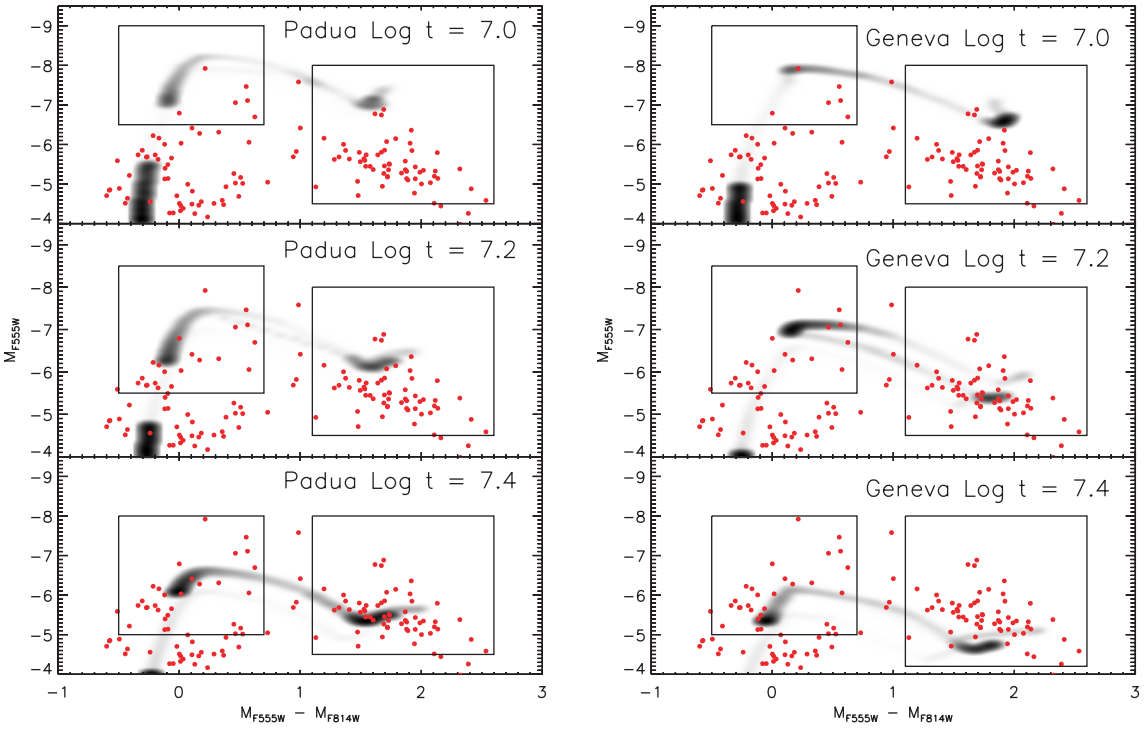

Figure 6. Hess diagrams for Padua (left-hand panel) and Geneva (right-hand panel) $Z = 0.008$ isochrones for three different ages. The filled circles (red in the online edition) are the observed CMDs for NGC 1569-B.

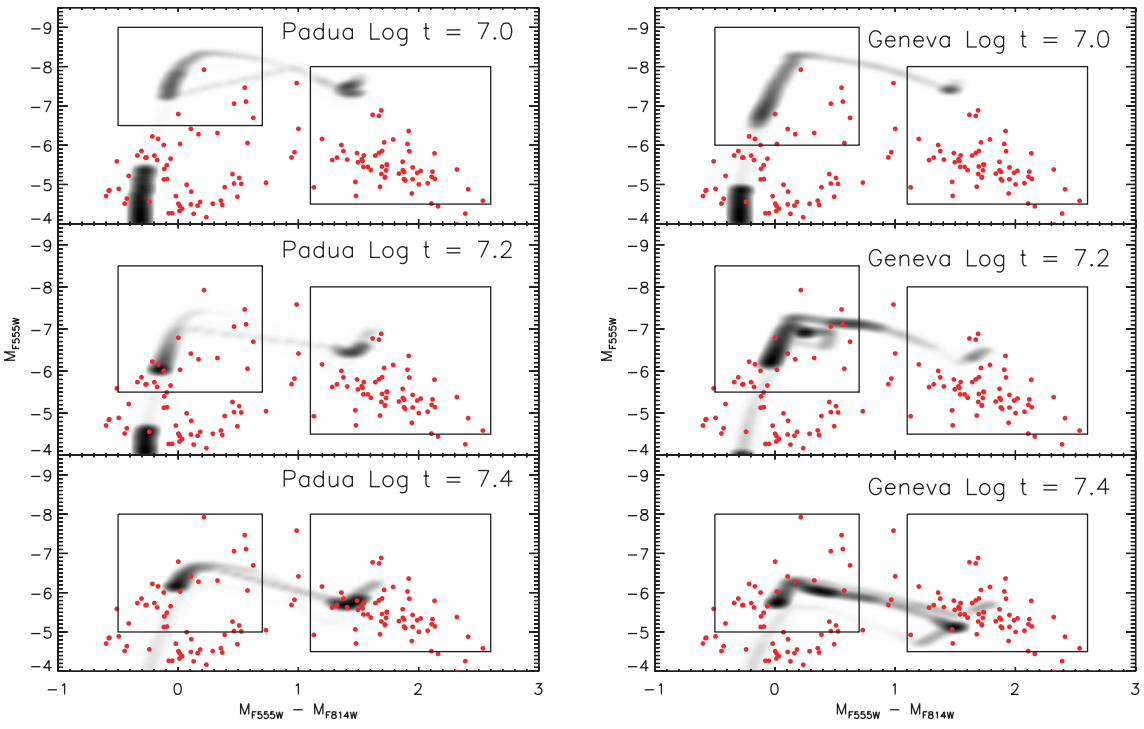

Figure 7. Same as Fig. 6 except that isochrones for $Z = 0.004$ are shown.

isochrones as lines connecting the model points, we plot synthetic Hess diagrams which show the density of stars predicted by the isochrones. The CMDs confirm that the best match to the RSGs is obtained for $Z = 0.008$ with a slightly younger age being preferred for the Geneva models ($\log t \sim 7.2$) than for the Padua models ($\log t \sim 7.4$). These ages are older than the estimate of $\log t = 7.1$ by Anders et al. (2004), based on integrated broad-band colours. However, if the distance of NGC 1569 is greater than we have assumed, then the absolute magnitude scale will shift accordingly, favouring a younger age. It seems that the CMD favours a metallicity for NGC 1569-B closer to $Z = 0.008$ than $Z = 0.004$, but we are reluctant to stress this point very strongly, given the large uncertainties in the stellar models for these young ages.

One specific 'amplifier' of the uncertainties in models for massive stars is the number ratio of blue supergiants (BSGs) and RSGs, as discussed in detail by Langer & Maeder (1995). While it is relatively straightforward to identify the RSGs in NGC 1569-B, it is, unfortunately, less clear how to select a sample of BSGs for comparison with the models as these are not clearly separated in the CMD. The Hess diagrams in Figs 6 and 7 provide some guidance and suggest that BSGs within the relevant age range should be brighter than $M_V \approx -5.5$. We therefore select BSG candidates within the left-hand box drawn in the bottom panel of Fig. 5. This results in 22 BSGs and 57 RSGs and thus a ratio of BSG/RSG $= 0.39 \pm 0.10$. In Table 2, we list the predictions by the Padua and Geneva models, obtained by counting the BSGs and RSGs within the boxes shown in Figs 6 and 7. We have used the same colour range as in Fig. 5, but adjusted the magnitude limits for each isochrone to avoid 'contamination' from main-sequence stars while making sure that the full range of BSG luminosities is covered in every case. Only the youngest $Z = 0.008$ Geneva isochrone can match the observed low BSG/RSG ratio, and in many of the other cases the discrepancy is very large, most notably for the metal-poor Geneva isochrones.

More generous selection limits for BSGs in the observed CMD will reduce the discrepancy, but in any case it is clear that the isochrones do not reproduce the observed CMD in detail. The problem of the BSG/RSG ratio will be addressed in more detail in forthcoming papers, using a larger sample of star clusters of different ages (see also Larsen 2007).

3.3 Structural Parameters and Dynamical Mass

3.3.1 Cluster size and its wavelength dependence

Having discussed the stellar content of NGC 1569-B, we now turn to a re-examination of its structural parameters and dynamical mass. We measured the size of the cluster in the ACS/HRC images using our ISHAPE code (Larsen 1999). The cluster size is determined by convolving a series of analytic model profiles with the PSF and varying the model parameters until the best fit is obtained. We used Elson, Fall & Freeman (1987; EFF) profiles of the form

$$I(R) = I_0 \left[1 + \left(\frac{r}{r_c}\right)^2\right]^{-\eta}, \quad (1)$$

where r_c is the core radius and η determines the steepness of the profile at large radii. Because neither the cluster itself nor the fitting profile has a clearly defined outer boundary, we experimented with various fitting radii up to 50 pixel (15 pc). Fig. 8 shows the image of the cluster, the best-fitting model, and the residuals for each band, for the largest fitting radius of 50 pixel. The resolution into individual stars means that the χ^2_ν values of the fits never get close to unity, but otherwise the models provide a good fit to the data.

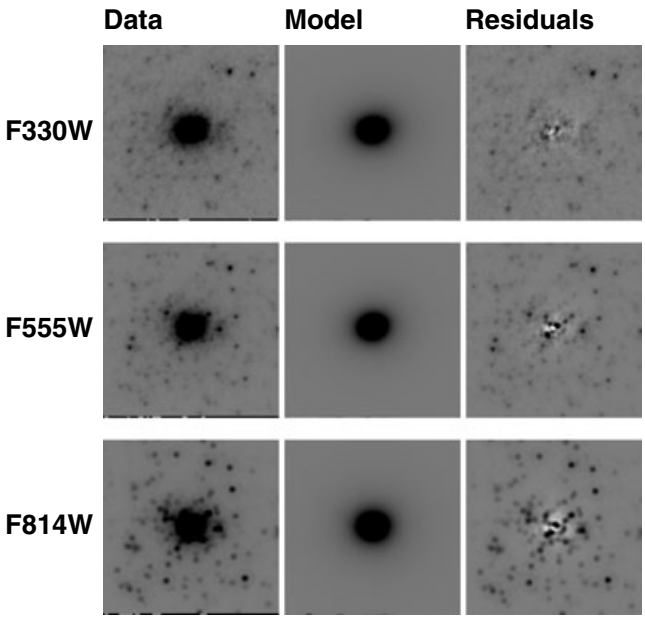

Figure 8. HRC images, ISHAPE model fits and residuals of NGC 1569-B in three passbands. These panels show a 100 × 100 pixel section, corresponding to 2.5 × 2.5 arcsec^2.

The PSFs used for the size measurements were based on DAOPHOT PSFs in the inner regions ($R < 5$ pixel). We know from the smooth residual images produced by the ALLFRAME photometry that these PSFs accurately represent the PSFs of our images. However, for the ISHAPE analysis we need to know the PSF at larger radii than for the photometry, and there the construction of accurate empirical PSFs becomes limited by decreasing S/N and non-uniformity of the background. For the analysis of structural parameters, we therefore made use of composite PSFs, constructed from the DAOPHOT PSFs for $R < 5$ pixel and using models computed by the TINYTIM package (Krist & Hook 1997) farther out.

Table 3 lists the full width at half-maximum (FWHM) along the major-axis, the minor-to-major axial ratio (B/A), the slope parameter η, and the half-light radius R_h for various fitting radii. All fits consistently yield an axial ratio of B/A ~ 0.8, confirming the conclusion from earlier work that NGC 1569-B is significantly elongated (O'Connell et al. 1994). For $\eta \leq 1$, the total luminosity of the model profile is infinite, and R_h is therefore undefined. For some fits, η is close to unity, leading to unreasonably large R_h values. We list two values for R_h: one assuming that the profile extends to infinity ($R_h(\infty)$) and another assuming that it is truncated at $R =$ 100 pixel ($R_h(100)$). For $\eta \gg 1$, the two R_h values are similar, but for $\eta \approx 1$ they differ substantially. The cut at $R = 100$ pixel (30 pc) is chosen fairly arbitrarily, apart from the fact that it is very difficult to trace the cluster profile to greater radii in the images.

Regardless of the fitting radius, all fits return a smaller FWHM at longer wavelengths. The formal errors on the FWHM values returned by ISHAPE are generally less than ±0.1 pixel, so the trend with wavelength appears significant. The FWHM is roughly equal to twice the core radius r_c of the EFF profiles (for $\eta = 1.0$ this holds exactly) so the trend in FWHM with wavelength is basically a trend in the core radius. Such a trend seems consistent with the finding of Hunter et al. (2000) that NGC 1569-B has redder $m_{F336W} - m_{F555W}$ colours near the centre. However, they also found that the $m_{F555W} - m_{F814W}$ colours become *bluer* near the centre. In the

Table 3. Structural parameters for NGC 1569-B. The FWHM and R_h are given in pixels [1 pixel = 0.025 arcsec = 0.27 pc (D/2.2 Mpc)].

	FWHM (pixels)	B/A	η	$R_h(\infty)$ (pixels)	$R_h(100)$ (pixels)
Fitrad=15 pixels					
F330W	4.72	0.77	1.16	20.02	8.32
F555W	4.27	0.82	1.30	6.98	5.72
F814W	3.68	0.86	1.32	5.72	4.92
Fitrad=20 pixels					
F330W	4.76	0.77	1.17	17.84	8.16
F555W	3.23	0.81	1.02	5×10^7	10.54
F814W	3.14	0.81	1.03	1.5×10^5	9.98
Fitrad=25 pixels					
F330W	5.33	0.75	1.31	8.07	6.56
F555W	4.54	0.79	1.32	6.79	5.72
F814W	3.68	0.81	1.18	12.64	6.66
Fitrad=35 pixels					
F330W	5.11	0.75	1.26	9.55	6.96
F555W	4.24	0.80	1.27	7.77	5.98
F814W	3.83	0.82	1.20	10.97	6.55
Fitrad=50 pixels					
F330W	4.78	0.75	1.14	27.08	8.76
F555W	3.81	0.79	1.16	16.34	7.17
F814W	3.19	0.86	1.10	50.64	7.95

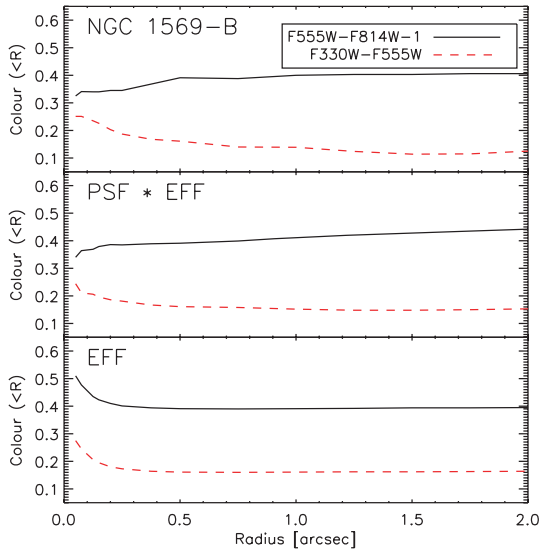

Figure 9. Top panel: $m_{F330W} - m_{F555W}$ and $m_{F555W} - m_{F814W}$ colour versus aperture size for NGC 1569-B. To fit the two plots on the same scale, 1 mag has been subtracted from $m_{F555W} - m_{F814W}$. Centre panel: same, but for the PSF in each filter convolved with EFF profiles of FWHM = 5.0, 4.5 and 4.0 pixel in *F330W*, *F555W* and *F814W*. The model profiles have been normalized to the same colour as the observed profiles at a radius of 0.5 arcsec. Bottom panel: same, but for the EFF profiles without any PSF convolution.

top panel of Fig. 9, we show the $m_{F330W} - m_{F555W}$ and $m_{F555W} - m_{F814W}$ colours versus aperture radius for NGC 1569-B measured on the HRC data. The trends seen in this plot are very similar to those observed by Hunter et al., with $m_{F330W} - m_{F555W}$ becoming redder inwards and $m_{F555W} - m_{F814W}$ getting bluer. How can this be consistent with a monotonic decrease in cluster core radius with wavelength?

The answer appears to be that a naïve comparison of colour gradients, as in Fig. 9, neglects the effect of the PSF. Colour gradients can result from a combination of changes with wavelength in the structure of *both* the cluster *and* the PSF. The PSF behaviour with wavelength is not monotonic. Due to the 'red halo' effect, more light is scattered to large radii at longer wavelengths, but the encircled energy distributions tabulated in Sirianni et al. (2005) also show that more light is scattered to intermediate radii (0.1–1 arcsec) in *F330W* relative to *F555W*. This is also illustrated by the fact that the aperture corrections to infinity display a minimum around 5000–6000 Å (fig. 10 in Sirianni et al. 2005).

To investigate this further, we convolved the PSF in *F330W*, *F555W* and *F814W* with EFF models for the respective filters having FWHM of 5.0, 4.5 and 4.0 pixel and envelope slopes of η = 1.26, 1.23 and 1.20 (guided by the numbers in Table 3). The centre panel of Fig. 9 shows the integrated colours versus aperture radius for these model profiles, normalized to match the observed colours at 0.5 arcsec. Although the intrinsic cluster core radius decreases monotonically with wavelength by design, we reproduce the observed trend towards bluer $m_{F555W} - m_{F814W}$ colours and redder $m_{F330W} - m_{F555W}$ colours near the centre. The bottom panel shows the colour–aperture relations for the pure EFF models, as they would be observed in the absence of any convolution with the PSF. In this case, both the $m_{F555W} - m_{F814W}$ and $m_{F330W} - m_{F555W}$ colours become redder near the centre. We conclude that the colour gradients observed by Hunter et al. (2000) (and also seen in the HRC data) are *consistent* with the monotonic decrease in the cluster FWHM with wavelength obtained from the ISHAPE fits.

Because the envelope slope η tends to be shallower at longer wavelengths, the correlation between FWHM and wavelength does not translate into a similarly strong trend of half-light radius R_h versus wavelength. The $R_h(\infty)$ values show a very large scatter while most $R_h(100)$ values are in the range 6–8 pixel or 0.15–0.20 arcsec. O'Connell et al. (1994) measured a half-light radius of R_h = 0.25 arcsec on *HST*/WFPC images, while Hunter et al. (2000) derived an almost identical value of R_h = 0.26 arcsec from *HST*/WFPC2 images. Our measurement on the ACS/HRC images is slightly smaller, but an increase in the cut-off radius by a factor of 2–3 would bring our R_h estimate into close agreement with previous studies. In the following, we therefore adopt $R_h = 0.20 \pm 0.05$ arcsec.

3.3.2 *Mass segregation?*

NGC 1569-B is not the only YMC in which the structure has been found to be wavelength-dependent. Larsen et al. (2001) noted that the colours of a YMC in NGC 6946 become bluer in larger apertures. A trend of smaller cluster size at longer wavelengths was also found for the cluster M82-F by McCrady, Graham & Vacca (2005), who argued that it might be due to mass-segregation (although this result has been questioned by Bastian et al. (2007) after a detailed analysis of the extinction near M82-F). Because the RSGs are the most-massive stars currently in the cluster, mass-segregation would cause them to be more centrally concentrated, making the cluster appear smaller at longer wavelengths where the RSGs dominate.

Mass-segregation may be either primordial in nature (the most-massive stars forming preferentially near the centre) or a result of dynamical evolution; in the latter case it is expected to occur on the

half-mass relaxation time-scale which is

$$t_{\rm rh} = \frac{1.7 \times 10^5 [R_{\rm h}({\rm pc})]^{3/2} N^{1/2}}{[m/{\rm M}_\odot]^{1/2}} \ {\rm yr}, \quad (2)$$

where N is the number of stars in the cluster and m is the mean mass per star (Spitzer 1987). For a total cluster mass of $\sim 4 \times 10^5$ M$_\odot$ (Section 3.3.5), a mean stellar mass of 0.6 M$_\odot$ (for a Kroupa IMF extending from 0.1 to 100 M$_\odot$) and $R_{\rm h} \approx 2$ pc, equation (2) yields $t_{\rm rh} \approx 5 \times 10^8$ yr, about a factor of 25 longer than the current age of NGC 1569-B. Thus, the cluster is not expected to be fully mass-segregated, but this statement is subject to a few caveats. Near the centre of the cluster, where the density is higher, the relaxation time will be shorter. Furthermore, massive stars can 'sink' to the centre on shorter time-scales due to energy equipartition. The time-scale for this to occur is inversely proportional to the mass of the stars in question (Gerhard 2000), so stars with masses characteristic of the current RSGs might become segregated on time-scales similar to the current age of NGC 1569-B. According to McMillan, Vesperini & Portegies Zwart (2007), dynamical mass-segregation may occur even more rapidly if a cluster forms from subclumps which already have some degree of primordial mass-segregation. Alternatively, mass-segregation may be imprinted in the structure of the cluster from the beginning (e.g. references in McMillan et al. 2007).

Whether or not mass-segregation can actually explain the observed relations between cluster structure and wavelength is another question. Fleck et al. (2006) calculated the difference Δ_{V-K} between the $V-K$ colour inside and outside the half-light radius for a mass-segregated cluster as a function of time and found this to be 0.05–0.15 mag. Using SSP models by Bruzual & Charlot (2003), we estimate $\Delta_{V-K}/\Delta_{V-I} \approx 2$, so we may expect mass-segregation to affect Δ_{V-I} by a few times 0.01 mag. From the data plotted in the bottom panel of Fig. 9, we measure a difference $\Delta_{V-I} = 0.03$ mag, which appears roughly consistent with the calculations by Fleck et al. Thus, it seems that mass-segregation *might* be responsible for the observed colour gradients, although it would be desirable to investigate this in more detail.

3.3.3 Integrated magnitude

For many of the same reasons that complicate measurements of the core- and half-light radius, the integrated magnitude of NGC 1569-B remains uncertain and a range of numbers can be found in the literature. Anders et al. (2004) list $M_{F555W} = -12.83$ for an $R = 0.46$ arcsec aperture. For their assumed distance of 2.2 Mpc, combined with reddening from Schlegel et al. and a correction for internal reddening in NGC 1569 of $E(B-V) = 0.05$ mag, this corresponds to $m_{F555W} = 16.30$. Origlia et al. (2001) list a reddening-corrected apparent magnitude of $m_{F555W,0} = 14.5$ or $m_{F555W} = 16.24$, close to the value given by Anders et al. Using a larger aperture of $R = 1.34$ arcsec, Hunter et al. (2000) list $M_{F555W} = -13.02$ for $E(B-V) = 0.56$ and a distance of $D = 2.5$ Mpc, that is, $m_{F555W} = 15.70$.

Most of the differences between published photometry can be ascribed to different choices of aperture radii. Using the same aperture radii, we can largely reproduce the numbers given above. For the apertures and background annuli used by Anders et al. (2004) and Hunter et al. (2000), we obtain $m_{F555W}(0.46\,{\rm arcsec}) = 16.20$ mag and $m_{F555W}(1.34\,{\rm arcsec}) = 15.66$ mag. Fig. 10 shows the integrated apparent m_{F555W} magnitude as a function of aperture radius, demonstrating that the curve-of-growth never levels off completely out to at least 2 arcsec. This is a generic difficulty for many young star clusters, which tend to have very extended outer envelopes with η-values close to 1 and hence poorly defined total luminosities (Larsen 2004).

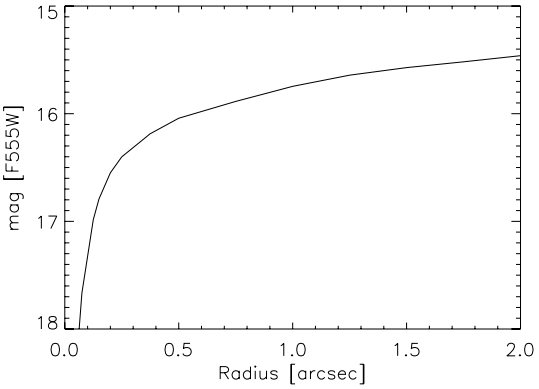

Figure 10. Integrated magnitude versus aperture radius for NGC 1569-B. The background was measured in an annulus between 2.0 and 3.0 arcsec.

As per definition, the total luminosity of the cluster should be twice that contained within the effective radius. We can therefore estimate the total integrated magnitude by measuring the magnitude within $R_{\rm h}$ and doubling the flux. From the data in Fig. 10, we get $m_{F555W} = 16.79/16.55/16.40$ mag in apertures of 0.15/0.20/0.25 arcsec. Doubling the fluxes, we then get $m_{F555W}(\infty) \approx 15.80 \pm 0.20$, where the quoted error is due to the uncertainty on the half-light radius. This is consistent with the measurement of Hunter et al. (2000) but brighter than measurements made in smaller apertures. However, this estimate of the integrated magnitude may still be a lower limit, because we have used a half-light radius that was already corrected for broadening by the PSF. In reality, some fraction of the cluster light is scattered from the centre to larger radii by the PSF, and we therefore expect that an aperture with the same radius as the intrinsic $R_{\rm h}$ will contain slightly *less* than half of the total cluster luminosity. By carrying out aperture photometry on a simulated PSF, we estimate this effect to be about 0.20 mag, consistent with the encircled energy tables in Sirianni et al. (2005). Our final estimate of the integrated cluster magnitude is then $m_{F555W}(\infty) \approx 15.60 \pm 0.20$.

3.3.4 Velocity dispersion

As noted in Section 3.1, the best fit of our RSG model spectrum to the NIRSPEC data requires a further broadening of 9.9 ± 1 km s^{-1} after accounting for the instrumental resolution. We have also derived the velocity dispersion using the standard cross-correlation technique (Tonry & Davis 1979; Ho & Filippenko 1996) applied in many previous studies. We refer to our previous papers on this subject for details (e.g. Larsen et al. 2001; Larsen & Richtler 2004; Larsen, Brodie & Hunter 2004). We used two template stars, HR 2184 (spectral class K1II) and HR 2235 (F5 II). Fig. 11 shows the cross-correlation function (CCF) for NGC 1569-B versus HR 2184 (thick curve) together with the CCF for the spectrum of HR 2235 (broadened by various amounts) versus that of HR 2184. The best match is obtained for a broadening of $\approx$10 km s^{-1}.

In Fig. 12, we show the distribution of velocity broadenings derived from the cross-correlation analysis in the various orders of the NIRSPEC spectrum and the different combinations of template stars. The best fits (highest CCF peaks) were obtained for orders 45, 46 and 49 and the results for these orders are shown as a filled

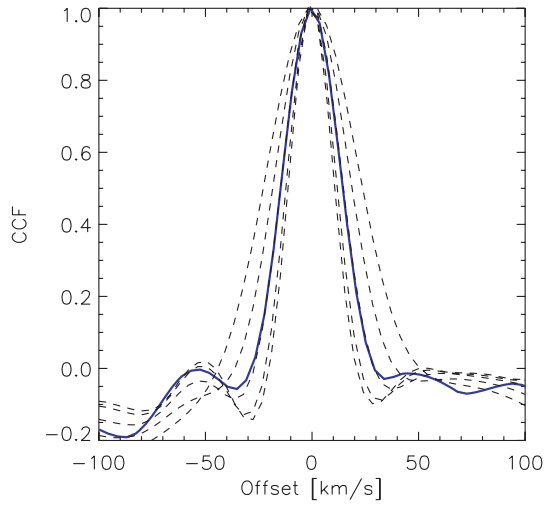

Figure 11. Cross-correlation functions for order 48 of the NIRSPEC data. The CCF for NGC 1569-B versus HR2184 is shown as a thick line (blue in the online edition). The thin dashed lines show the CCF for HR2235 versus HR2184, with the spectrum of HR2235 being broadened by 1, 5, 10, 15 and 20 km s^{-1}. The narrowest CCF peaks correspond to the smallest amount of broadening. All CCFs have been shifted to a mean of 0 km s^{-1} for easier comparison.

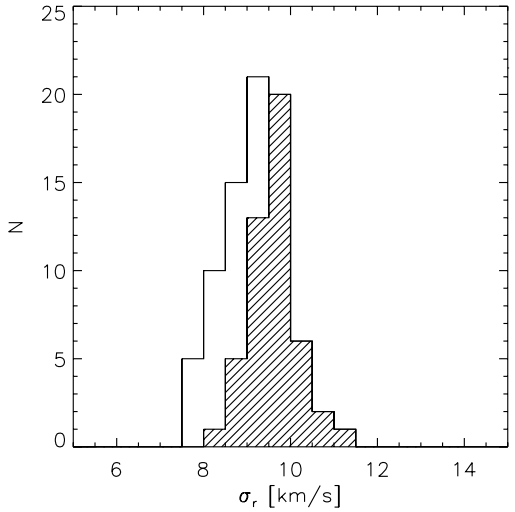

Figure 12. Distribution of velocity dispersion measurements from the cross-correlation analysis. The filled histogram shows the measurements based on the best orders (45, 46, 49) while the outlined histogram also includes orders 47 and 48. The best orders yield a mean of $\sigma_r = 9.6 \pm 0.1$ km s^{-1}.

histogram. The mean is $\sigma_r = 9.6 \pm 0.1$ km s^{-1}. If we include orders 47 and 48, the mean decreases to $\sigma_r = 9.2 \pm 0.1$ km s^{-1}, still significantly greater than 7.5 km s^{-1} measured by Gilbert & Graham (2002). For the following discussion, we will adopt $\sigma_r = 9.6 \pm 0.3$ km s^{-1}, including the estimate of σ_r from the RSG model fit within our 1σ error.

3.3.5 Dynamical mass

Assuming virial equilibrium and that mass traces light, the cluster mass is related to the one-dimensional velocity dispersion σ_r and half-light radius by

$$M_{\rm vir} = \alpha \frac{\sigma_r^2 R_h}{G} \quad (3)$$

with $\alpha \approx 9.75$. Inserting the R_h and σ_r values derived in Sections 3.3.1 and 3.3.4 (summarized in Table 4), we obtain a dynamical mass of $M_{\rm vir} = (4.4 \pm 1.1) \times 10^5$ M$_\odot$ which is about a factor of 2 higher than the value of 2.3×10^5 M$_\odot$ derived by Gilbert & Graham (2002). The difference is mostly due to our greater velocity dispersion. Note that $M_{\rm vir}$ scales linearly with R_h, and thus with the assumed distance D. Rather than trying to include an uncertainty on the distance, we have specified this dependency explicitly for the cluster mass listed in Table 4. This dynamical mass of NGC 1569-B is much greater than for any young star cluster currently known in the Milky Way and also well above the median mass of old globular clusters (though still comfortably within the mass range of Milky Way globular clusters).

Table 4. A summary of properties of NGC 1569-B. R_h is the half-light radius, m_{F555W} is our estimated total apparent magnitude in the *F555W* band, σ_r is the projected velocity dispersion, v_r the heliocentric radial velocity, $M_{\rm vir}$ is the dynamical mass and ρ_h is the mean density within the half-mass radius. For quantities that depend on the assumed distance, this dependency is specified explicitly.

R_h (arcsec)	0.20 ± 0.05 arcsec
m_{F555W} (VEGAMAG)	15.60 ± 0.20
σ_r (km s^{-1})	9.6 ± 0.3
v_r (km s^{-1})	-78 ± 3
R_h (pc)	$(2.1 \pm 0.5)\,(D/2.2\,{\rm Mpc})$
$M_{\rm vir}$ (M$_\odot$)	$(4.4 \pm 1.1)\,10^5\,(D/2.2\,{\rm Mpc})$
ρ_h (M$_\odot$ pc^{-3})	$(2.5 \pm 1.3)\,10^3\,(D/2.2\,{\rm Mpc})^{-2}$

We can compare the dynamical mass estimate with the mass expected for a cluster of this age and luminosity, given a normal stellar IMF. For $Z = 0.008$ and a Chabrier IMF, the Bruzual & Charlot (2003) SSP models predict a *V*-band absolute magnitude of $M_V = 1.53 \pm 0.15$ mag M$_\odot^{-1}$ for $\log t = 7.3 \pm 0.1$. For $M_V \approx m_{F555W} - 26.7 - A_V = -12.85 \pm 0.2$, the 'photometric' mass is then $(5.5 \pm 1.3) \times 10^5$ M$_\odot$, which is in agreement with the dynamical mass within the 1σ errors.

The close agreement between the dynamical and photometric mass estimates is probably somewhat fortuitous, given the uncertainties on the distance, reddening and age. In the absence of reddening, the dynamical-to-photometric mass ratio will scale as $1/D$. However, since the problems of determining the reddening and distance to NGC 1569-B are closely tied, the comparison is not as straightforward. To first order, the absolute magnitude of NGC 1569-B may be roughly independent of the reddening correction, since most distance determinations to NGC 1569 are based on standard candles. The dynamical-to-photometric mass ratio will then scale as D instead of $1/D$. All this neglects any possible dependency of the age estimate on distance and reddening. This will depend on the method used for age determination – ages based on integrated colours (or spectroscopy) will be distance-independent and probably only weakly dependent on the reddening (since this is usually included as a free parameter in the fit) while CMD-based ages will depend on both.

Another source of uncertainty is the parameter α in equation (3). In a mass-segregated cluster, α will have a different value from that we have assumed. Because of energy equipartition, the massive stars will acquire lower velocities and sink to the centre. Since *measurements* of the velocity dispersion and cluster size based on

integrated light are dominated by these stars, the mass derived from equation (3) will be underestimated. Fleck et al. (2006) model the evolution of α for dynamically mass-segregated star clusters and give an analytical approximation to the relative error $\Delta\alpha/\alpha$ as a function of age and relaxation time. For an age of 20 Myr and $t_{\rm rh} = 500$ Myr, their equation (31) yields $\Delta\alpha/\alpha \approx 13$ per cent. With this correction, the dynamical mass becomes $M_{\rm vir,corr} = (4.9 \pm 1.2) \times 10^5$ M$_\odot$ for $D = 2.2$ Mpc, that is, even in even closer agreement with the photometric estimate.

4 DISCUSSION AND SUMMARY

We have presented a detailed investigation of the stellar content and other properties of the massive star cluster 'B' in NGC 1569. Using new high S/N *H*-band echelle spectroscopy from the NIRSPEC spectrograph on Keck II, we have carried out abundance analysis of RSG stars in the cluster. We find an iron abundance of [Fe/H] $= -0.63 \pm 0.08$, close to that of SMC field stars. Our estimate of the oxygen abundance, [O/H] $= -0.29 \pm 0.07$, is about a factor of 2 higher than that derived for H II regions (Storchi-Bergmann et al. 1994; Devost et al. 1997; Kobulnicky & Skillman 1997), and the resulting supersolar [O/Fe] abundance is unlike that observed in the Magellanic Clouds and young stellar populations in the Milky Way. However, according to our measurements NGC 1569-B also differs from these galaxies by having a higher [α/Fe] ratio. The difference between our [O/H] measurement for NGC 1569-B and the O abundance derived for H II regions is greater than the formal uncertainties on either value, and our oxygen abundance is higher than the nebular abundances in most dwarf galaxies (e.g. Vaduvescu, McCall & Richer 2007). This raises the question whether one (or both) methods suffer from possible systematic errors, or if there might be a genuine difference between cluster and H II region abundances in NGC 1569 – perhaps due to an *ab initio* oxygen enhancement of the gas out of which the cluster formed. Since oxygen is the only element in common between the cluster and H II region data, a detailed comparison of the abundance patterns is unfortunately not possible. However, it is of interest to note that the very strong Wolf–Rayet features in the spectrum of cluster A also suggest a high metallicity (Maoz et al. 2001).

NGC 1569 is a popular target for testing models of chemical evolution, and it is generally recognized that the strong galactic wind observed in the galaxy must play an important role. Martin, Kobulnicky & Heckman (2002) observed a supersolar [α/Fe] ratio for the wind, as we do for NGC 1569-B. However, it is unclear to what extent the two are related as material ejected in the outflow may not participate in star formation, and in any case not before it has had time to cool down and fall back into the galaxy. The chemical evolution of an NGC 1569-type galaxy has been modelled in detail by Recchi et al. (2006), assuming a variety of bursty star formation histories. Their chemodynamical simulations show that elements produced in the last burst of star formation generally do not get mixed with the interstellar medium in the galaxy, but instead get injected into the hot gas phase. None of their models produce an O abundance as high as the one observed by us, and the model that comes closest [$12 + \log({\rm O/H}) \sim 8.4$] severely underpredicts the N/O abundance of the H II regions observed by Kobulnicky & Skillman (1997). Generally, the best fits to the H II region abundances are obtained for a 'gasping' star formation history, but these models all predict a maximum $12 + \log({\rm O/H}) \approx 8.1$. Similarly, the O abundance predicted by the models of Romano, Tosi & Matteucci (2006) for NGC 1569 never exceeds $12 + \log({\rm O/H}) = 8.41$. We speculate that the galactic wind which is responsible for removing metals may be less efficient in doing so near the bottom of the potential well where the massive clusters formed. Unfortunately, none of the models includes predictions for the wide range of other elements we are observing here.

The SMC presents an interesting comparison case. Early spectroscopic studies and Strömgren photometry indicated that the young cluster NGC 330 is about 0.5 dex more metal-poor than the surrounding field (Grebel & Richtler 1992 and references therein). High-dispersion spectroscopy by Hill (1999) showed a smaller and only marginally significant difference between the field stars and NGC 330, although still in the sense that the cluster is more metal-poor than the field ([Fe/H] $= -0.82 \pm 0.10$ versus [Fe/H] $= -0.69 \pm 0.11$). The [O/Fe] abundance ratios in these stars were all found to be subsolar ([O/Fe] ≈ -0.15 to -0.3 dex), as in the LMC and in young Galactic supergiants (Hill, Barbuy & Spite 1997). Hill (1999) also found the α-element abundances (Mg, Ca, Ti) relative to Fe to be around solar for NGC 330. Gonzalez & Wallerstein (1999) found slightly lower iron abundances of [Fe/H] $= -0.94 \pm 0.02$ for K supergiants in NGC 330 than Hill (1999) and an [O/Fe] ratio closer to solar. They derived somewhat enhanced [Ca/Fe], [Si/Fe] and [Mg/Fe] ratios ($+0.18$, $+0.32$ and $+0.11$), in contrast to subsolar ratios derived for B stars.

While there is some evidence for a difference in metallicity between NGC 330 and the SMC field, the situation there seems to be in contrast with the case of NGC 1569-B where we find a *higher* oxygen abundance of the cluster compared to the H II regions and an *enhanced* [O/Fe] ratio. Our mean [α/Fe] $= +0.31 \pm 0.09$ is also higher than that derived for the stars in NGC 330. One significant difference may be the mass of NGC 1569-B, which is probably an order of magnitude greater than that of NGC 330 (Feast & Black 1980).

The spectral analysis returns a mean $T_{\rm eff} = 3800 \pm 200$ K and $\log g \approx 0.0$ for the RSGs in NGC 1569-B. We have checked these values using resolved photometry of the RSGs in the cluster, derived from archival *HST*/ACS images. About 60 RSGs are easily identifiable in the CMD, and from their $m_{F555W} - m_{F814W}$ colours we derive a mean effective temperature of $\langle T_{\rm eff}\rangle = 3850$ K and $\log g = 0.1$. An even closer match to the spectroscopic $T_{\rm eff}$ is obtained if we weigh the $T_{\rm eff}$ estimates for the individual stars by their *H*-band luminosities, in which case we get $\langle T_{\rm eff}\rangle = 3790$ K.

We have compared the CMD with $Z = 0.004$ and 0.008 isochrones from the Padua and Geneva groups. Both sets of models provide the best match to the observed colours and magnitudes of the RSGs for $Z = 0.008$ and ages of 15–25 Myr, but no isochrone can reproduce the observed CMD in detail. For these subsolar metallicities, the models predict higher (by up to a few 100 K) mean effective temperatures $\langle T_{\rm eff}\rangle$ for the RSGs than observed. Since the RSGs generally become cooler with increasing metallicity, models of higher metallicity are favoured, but models of solar metallicity would be required to match the observed colours. For such models, however, the *blue* supergiants become much too cool to match the observations. The observed ratio of BSGs to RSGs (BSG/RSG $= 0.39 \pm 0.10$) is also significantly lower than most of the model predictions. Although we are detecting an impressive number of RSGs, it should be noted that since we are only resolving stars located well outside the half-light radius, the actual number of RSGs in NGC 1569-B is likely to be more than a factor of 2 greater than the number we have detected.

We derive a velocity dispersion of 9.6 ± 0.3 km s^{-1} from the integrated spectrum of NGC 1569-B, somewhat higher than the value of 7.5 km s^{-1} of Gilbert & Graham (2002). Combining this with an estimate of the cluster half-light radius of 0.20 ± 0.05 arcsec

measured on the ACS images, we obtain a dynamical mass of $(4.4 \pm 1.1) \times 10^5 (\frac{D}{2.2\,\mathrm{Mpc}})\,\mathrm{M}_\odot$. This is in excellent agreement with the mass predicted by SSP models for a cluster of this age and luminosity and a standard IMF. A correction for mass-segregation would bring the two estimates into even closer agreement.

Our analysis of structural parameters reveals a decrease in core radius with wavelength for NGC 1569-B. This trend is consistent with the colour gradients observed by Hunter et al. (2000) and by us in the HRC data when variations in the PSF are taken into account. A similar colour gradient was observed in an YMC in NGC 6946 (Larsen et al. 2001). The correlation between core radius and wavelength is also in the same sense as that found for M82-F by McCrady et al. (2005) and may be an indication that mass-segregation (primordial or dynamical) is present in NGC 1569-B. However, this needs to be confirmed by a more detailed analysis, including a modelling of how mass-segregation would translate into observables such as core- and half-light radius.

As a final note, we find it fascinating to contemplate that only a couple of decades ago, it was still uncertain whether NGC 1569-A and NGC 1569-B were in fact star clusters in NGC 1569 or mere foreground stars. Today, the ACS onboard *HST* has made it possible to not only settle this question definitively, but also to study the individual stars that make up these clusters.

ACKNOWLEDGMENTS

SSL thanks the International Space Science Institute (ISSI) in Bern, Switzerland, where part of this work was done, for its hospitality. Mark Gieles and Evghenii Gaburov are thanked for interesting discussions about the effect of mass-segregation on integrated colours. JB acknowledges support from NSF grant AST-0206139. We acknowledge the Keck Observatory and the NIRSPEC team. The authors wish to recognize and acknowledge the very significant cultural role and reverence that the summit of Mauna Kea has always had within the indigenous Hawaiian community. We are most fortunate to have the opportunity to conduct observations from this mountain.

REFERENCES

Anders P., de Grijs R., Fritze-v.Alvensleben U., Bissantz N., 2004, MNRAS, 347, 17
Arp H., Sandage A., 1985, AJ, 90, 1163
Bastian N., Konstantopoulos I., Smith L. J., Trancho G., Westmoquette M. S., Gallagher J. S., 2007, MNRAS, 379, 1333
Bessel M. S., Castelli F., Plez B., 1998, A&A, 333, 231
Bièmont E., Grevesse N., 1973, Atomic Data and Nuclear Data Tables, 12, 221
Bruzual G., Charlot S., 2003, MNRAS, 344, 1000
Burstein D., Heiles C., 1982, AJ, 87, 1165
Clark J. S., Negueruela I., Crowther P. A., Goodwin S. P., 2005, A&A, 434, 949
de Marchi G., Clampin M., Greggio L., Leitherer C., Nota A., Tosi M., 1997, ApJ, 479, L27
de Vaucouleurs G., de Vaucouleurs A., Corwin Jr. H. G., Buta R. J., Paturel G., Fouque P., 1991, Third Reference Catalogue of Bright Galaxies. Springer-Verlag, New York
Devost D., Roy J.-R., Drissen L., 1997, ApJ, 482, 765
Elson R. A. W., Fall S. M., Freeman K. C., 1987, ApJ, 323, 54
Feast M. W., Black C., 1980, MNRAS, 191, 285
Figer D. F., MacKenty J. W., Robberto M., Smith K., Najarro F., Kudritzki R. P., Herrero A., 2006, ApJ, 643, 1166
Fleck J.-J., Boily C. M., Lançon A., Deiters S., 2006, MNRAS, 369, 1392
Gerhard O., 2000, in Lançon A., Boily C. M., eds, ASP Conf. Ser. Vol. 211, Massive Stellar Clusters. Astron. Soc. Pac., San Francisco, p. 12
Gilbert A. M., Graham J. R., 2002, in Geisler D., Grebel E. K., Minniti D., eds, IAU Symp. 2007, Extragalactic Star Clusters. Astron. Soc. Pac., San Francisco, p. 471
Girardi L., Bressan A., Bertelli G., Chiosi C., 2000, A&AS, 141, 371
Gonzalez G., Wallerstein G., 1999, AJ, 117, 2286
Gonzalez G., Wallerstein G., 2000, AJ, 119, 1839
Grebel E., Richtler T., 1992, A&A, 253, 359
Grevesse N., Sauval A. J., 1998, Space Sci. Rev., 85, 161
Hauschildt P. H., Allard F., Ferguson J., Baron E., Alexander D. R., 1999, ApJ, 525, 871
Hill V., 1999, A&A, 345, 430
Hill V., Barbuy B., Spite M., 1997, A&A, 323, 461
Ho L. C., Filippenko A. V., 1996, ApJ, 466, L83
Hunter D. A., O'Connell R. W., Gallagher J. S., Smecker-Hane T. A., 2000, AJ, 120, 2383
Israel F. P., 1988, A&A 194, 24
Johnson H. R., Bernat A. P., Krupp B. M., 1980, ApJS, 42, 501
Koekemoer A. M., Fruchter A. S., Hook R. N., Hack W., 2002, in Arribas S., Koekemoer A., Whitmore B. C., eds, The 2002 HST Calibration Workshop. STScI, Baltimore, MD, USA, p. 337
Kobulnicky H. A., Skillman E. D., 1997, ApJ, 489, 636
Krist J., Hook R., 1997, "The Tiny Tim User's Guide". STScI, Baltimore, MD, USA
Kroupa P., 2002, Sci, 295, 82
Lambert D. L., Tomkin J., 1974, ApJ, 194, L89
Langer N., Maeder A., 1995, A&A, 295, 685
Larsen S. S., 1999, A&AS, 139, 393
Larsen S. S., 2004, A&A, 416, 537
Larsen S. S., 2007, in De Marchi G., Macchetto F. D., eds, Proc. 41st ESLAB Symp., The Impact of HST on European Astronomy. Springer-Verlag, Berlin, preprint (astro-ph/0707.0205)
Larsen S. S., Richtler T., 2004, A&A, 427, 495
Larsen S. S., Brodie J. P., Elmegreen B. G., Efremov, Yu. N., Hodge P. W., Richtler T., 2001, ApJ, 556, 801
Larsen S. S., Brodie J. P., Hunter D. A., 2004, AJ, 128, 2295
Larsen S. S., Origlia L., Brodie J. P., Gallagher J. S., III, 2006, MNRAS, 368, L10
Lejeune T., Schaerer D., 2001, A&A, 366, 538
McCrady N., Graham J. R., Vacca W. D., 2005, ApJ, 621, 278
McLean I. S. et al., 1998, in Fowler A. M., ed., Proc. SPIE, Vol. 3354, Infrared Astronomical Instrumentation. SPIE, Bellingham, p. 566
McMillan S. L. W., Vesperini E., Portegies Zwart S. F., 2007, ApJ, 655, L45
Makarova L. N., Karachentsev I. D., 2003, Astrophysics, 46, 144
Maoz D., Ho L. C., Sternberg A., 1998, ApJ, 554, L139
Martin C. L., Kobulnicky H. A., Heckman T. M., 2002, ApJ, 574, 663
Mayall N. U., 1935, PASP, 47, 319
Meléndez J., Barbuy B., 1999, ApJS, 124, 527
O'Connell R. W., Gallagher J. S., III, Hunter D. A., 1994, ApJ, 433, 65
Origlia L., Leitherer C., 2000, AJ, 119, 2018
Origlia L., Oliva E., 2000, New Astron. Rev., 44, 257
Origlia L., Moorwood A. F. M., Oliva E., 1993, A&A, 280, 536
Origlia L., Leitherer C., Aloisi A., Greggio L., Tosi M., 2001, AJ, 122, 815
Origlia L., Rich R. M., Castro S., 2002, AJ, 123, 1559
Origlia L., Ferraro F. R., Bellazzini M., Pancino E., 2003, ApJ, 591, 916
Recchi S., Hensler G., Angeretti L., Matteucci F., 2006, A&A, 445, 875
Rolleston W. R. J., Trundle C., Dufton P. L., 2002, A&A, 396, 53
Romano D., Tosi M., Matteucci F., 2006, MNRAS, 365, 759
Schaller G., Schaerer D., Meynet G., Maeder A., 1992, A&AS, 96, 269
Schlegel D. J., Finkbeiner D. P., Davis M., 1998, ApJ, 500, 525
Sirianni M. et al., 2005, PASP, 117, 1049
Spitzer L., 1987, Dynamical Evolution of Globular Clusters. Princeton Series in Astrophysics

Sternberg A., 1998, ApJ, 506, 721
Stetson P. B., 1987, PASP, 99, 191
Stetson P. B., 1990, in Worrall D. M., Biemesderver C., Barnes J., eds, ASP Conf. Ser. Vol. 25, Astronomical Data Analysis Software and Systems I. Astron. Soc. Pac., San Francisco, p. 297
Storchi-Bergmann T., Calzetti D., Kinney A. L., 1994, ApJ, 429, 572
Tomkin J., Luck R. E., Lambert D. L., 1976, ApJ, 210, 694
Tonry J., Davis M., 1979, AJ, 84, 1511
Vaduvescu O., McCall M. L., Richer M. G., 2007, AJ, 134, 604
van den Bergh S., 1999, PASP, 111, 1248

This paper has been typeset from a TEX/LATEX file prepared by the author.